

tation of the TBP groups around the phenyl-porphyrin  $\sigma$  bond. In terms of the mechanics of motion, rotation of the rear TBP side groups is blocked by the tip, whereas the front TBP side groups show uncorrelated oscillatory lateral and torsional motions. The former effect produces an opening of the angle between the two front TBP groups from  $90^\circ$  to  $\sim 115^\circ$  (Fig. 4C, top). The resulting translational motion resembles a “slip-stick”-type action of the individual TBP side groups with the surface (Fig. 4C, bottom). This uncorrelated slip-stick action of the individual legs effectively lowers the barrier for lateral displacement as compared with that of a rigid molecule—a crucial aspect of the nanomechanics of movement for this molecule. This mechanism is characteristically different from sliding processes used for low-temperature manipulation (9).

The control of internal molecular mechanics and of interactions between the molecule and the surface is a prerequisite for selective positioning and assembly. We have demonstrated that functional groups attached to a rigid planar molecule can

maintain thermally stable bonding, while being sufficiently labile to facilitate tip-induced translation without rupturing internal molecular bonds. We propose this conceptual approach of specific functionalization to separate substrate-molecular interactions as a step that goes beyond current approaches of engineering on the molecular scale.

#### REFERENCES AND NOTES

1. C. F. Quate, in *Highlights in Condensed Matter Physics and Future Prospects*, NATO ASI Series B (Plenum, New York, 1991), vol. 285, pp. 573–630; H. Rohrer, in *Nanosources and Manipulation of Atoms Under High Fields and Temperatures: Applications*, V. T. Binh *et al.*, Eds. (Kluwer, Dordrecht, 1993), vol. 235, pp. 1–12; J. A. Stroscio and D. M. Eigler, *Science* **254**, 1319 (1991).
2. D. M. Eigler and E. K. Schweizer, *Nature* **344**, 524 (1990); M. F. Crommie, C. P. Lutz, D. M. Eigler, *Science* **262**, 218 (1993); G. Meyer, B. Neu, K. H. Rieder, *Appl. Phys. A* **60**, 343 (1995).
3. R. Gaisch *et al.*, *Ultramicroscopy* **42–44**, 1621 (1992).
4. P. Sautet and C. Joachim, *Chem. Phys. Lett.* **185**, 23 (1991); *Surf. Sci.* **271**, 387 (1992); C. Chavy, C. Joachim, A. Altibelli, *Chem. Phys. Lett.* **214**, 569 (1993).
5. T. A. Jung, R. R. Schlittler, J. K. Gimzewski, unpublished data.

6. J. K. Gimzewski, R. Berndt, R. R. Schlittler, *Phys. Rev. B* **45**, 6844 (1992).
7. Manipulation software was developed in collaboration with M. E. Welland, M. Murrell, and T. Wong (University of Cambridge) under the European Union ESPRIT basic research project PRONANO (project number 8523).
8. J. K. Gimzewski, S. Modesti, T. David, R. R. Schlittler, *J. Vac. Sci. Technol. B* **12**, 1942 (1994); P. H. Beton, A. Dunn, P. Moriarty, *Appl. Phys. Lett.* **67**, 1075 (1995).
9. X. Bouju, C. Joachim, C. Girard, P. Sautet, *Phys. Rev. B* **47**, 7454 (1993); D. M. Eigler, C. P. Lutz, W. E. Rudge, *Nature* **352**, 600 (1991); R. E. Walkup, D. M. News, P. Avouris, *Phys. Rev. B* **48**, 1858 (1993); N. D. Lang, *ibid.* **49**, 2067 (1994).
10. H. Song, C. A. Reed, W. R. Scheidt, *J. Am. Chem. Soc.* **111**, 6865 (1989); B. S. Erler, W. F. Scholz, Y. J. Lee, W. R. Scheidt, C. A. Reed, *ibid.* **109**, 2644 (1987); T. K. Miyamoto, N. Sugita, Y. Matsumoto, Y. Sasaki, M. Konno, *Chem. Lett. (Japan)* (1983), p. 1695.
11. We thank P. Guéret and H. Rohrer for enlightening and helpful discussions, M. E. Welland for valuable conversations, and T. Takami for providing the molecules used in this study. We gratefully acknowledge partial support by the Bundesamt für Bildung und Wissenschaft of Switzerland through the European Union ESPRIT basic research project PRONANO (8523). C.J. and H.T. thank the Région Midi-Pyrénées and the CNRS Groupement de Recherche NanoMips (1145) for financial support during this work.

29 September 1995; accepted 13 November 1995

## The Shape of Mars and the Topographic Signature of the Hemispheric Dichotomy

David E. Smith and Maria T. Zuber

Reanalysis of occultation data from the Mariner 9 and Viking Orbiter spacecraft to determine the shape of Mars indicated that the hemispheric dichotomy is not a fundamental feature of the shape of the planet. It is a consequence of an approximately 3-kilometer offset between Mars's center of mass and center of figure, and the boundary, along most of its length, consists of broad, gradual surface slopes over distances of thousands of kilometers. This result was supported by analysis of high spatial resolution Earth-based radar topographic profiles. Any successful model for the origin of the dichotomy must explain a planet with an ellipsoidal shape and a long wavelength gradual topographic transition between the northern and southern hemispheres.

The surface of Mars is distinctly different in the northern and southern hemispheres. The south is old and heavily cratered, whereas the north is younger and lightly cratered and was probably volcanically resurfaced early in Mars's history (1, 2). This hemispheric dichotomy is characterized by a geologic boundary between the hemispheres that is expressed as knobby and fretted terrains and detached plateaus (2–4) distributed over a relatively limited width of  $\sim 700$  km (5). Along the boundary, eleva-

tions have been interpreted to decrease from south to north by  $\sim 1$  to 3 km (1, 6, 7), and the change in topography has been correlated with geologic features (8).

The formation of the dichotomy has been attributed to internal processes, such as postaccretionary core formation (9), and to crustal delamination (in the northern hemisphere) and underplating (in the southern hemisphere) by vigorous mantle convection (10). It has also been proposed that the low northern hemisphere was the result of a massive impact (5, 11) or impacts (12), and this region may have been the site of an early martian ocean (13). The lack of gravity anomalies along the boundary (14) may indicate thick crust beneath the southern highlands and thinner crust beneath the northern lowlands (1, 15).

In addition, the boundary region has been proposed as the site of relic plate boundaries (16). Consequently, understanding the origin of the hemispheric difference has implications for the evolution and internal structure of Mars.

Most analyses of the origin of the dichotomy have been based on global topographic models (8) with poor long-wavelength accuracy (17). The topography has also been studied by means of higher spatial resolution measurements derived from photogrammetry, stereo imaging, and ultraviolet spectra (7, 18). Although these methods yield information on relative heights within an individual image frame or mosaic, the heights cannot be placed in a global reference frame and are of limited utility in relating local structure to global structure.

Radio occultation measurements (19–22) provide estimates of the radius of the planet at the time (and location) when the radio signal from a spacecraft is lost (occulted) behind the planet or emerges from behind the planet in its orbit (23). Occultation data formed the basis of several early determinations of Mars's topography (21, 22, 24) and were included in more recent U.S. Geological Survey (USGS) digital elevation models (DEMs) (8), but the data have not been analyzed since the 1970s. Here, we reanalyzed these data by using improved spacecraft orbital information (25), the latest planetary ephemerides and dynamical information (26), and revised atmospheric refraction correc-

D. E. Smith, Laboratory for Terrestrial Physics, NASA/Goddard Space Flight Center, Greenbelt, MD 20771, USA.

M. T. Zuber, Department of Earth, Atmospheric and Planetary Sciences, Massachusetts Institute of Technology, Cambridge, MA 02139–4307, USA, and Laboratory for Terrestrial Physics, NASA/Goddard Space Flight Center, Greenbelt, MD 20771, USA.

tions (27) to improve the spatial location of occultation points on the martian surface as well as the occultation radii with respect to Mars's center of mass (COM). In addition, we referenced the data to an equipotential surface (28), rather than to

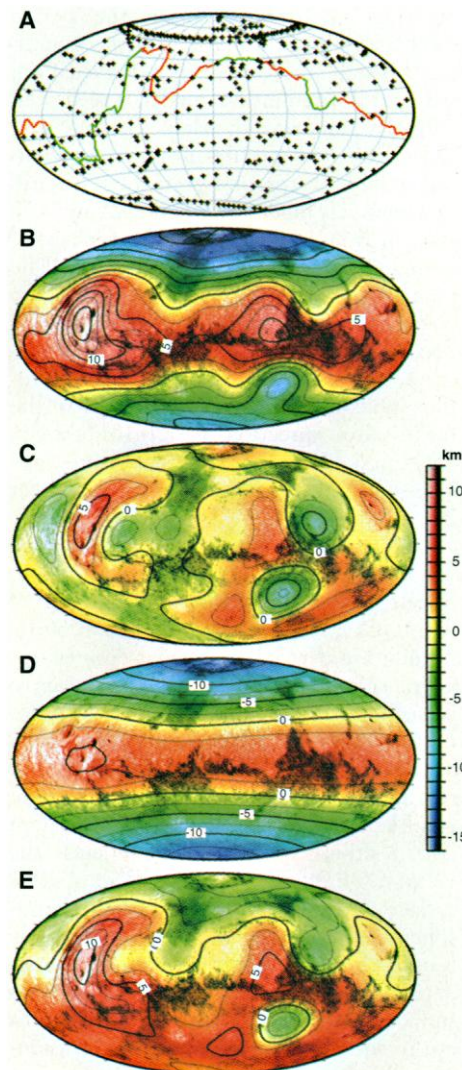


**Fig. 1.** (A) Locations of topography measurements of Mars. Black crosses show positions of occultation points and two Viking lander sites. The red lines show the location of the geologic boundary scarp as denoted on the USGS geologic map of Mars (4, 5); the green lines show the approximate location of the dichotomy in areas where no boundary scarp is mapped. (B) Shape of Mars as derived from the data in (A). (C) Ellipsoidal heights, which are residuals between the occultation radii and the best-fit reference ellipsoid (47). (D) Geoid of Mars from the GMM-1 (Goddard Mars Model-1) gravitational field model (38). (E) Geopotential topography of Mars. (B) through (E) are eighth-degree and order spherical harmonic models with a half-wavelength spatial resolution of 1350 km. All of the calculations used a mass-centered coordinate system and areocentric coordinates with an east positive longitude convention. For all maps, the cartographic projection is Mollweide with zero longitude at the center of each map.

a 6.1-mbar surface derived from an earlier degree-4 gravity model (29).

The locations (latitudes, longitudes, and radii) of the Viking 1 and 2 Lander sites (30) were added to the occultation radii. Using the occultation and lander data (Fig. 1A), we solved for a best-fit topographic reference ellipsoid (31). This ellipsoid has a root-mean-square (rms) fit of 1.9 km to all the data, and its center is offset from Mars's COM by  $3561 \pm 100$  m, of which  $3081 \pm 60$  m is down the  $z$  axis, such that the south pole is  $\sim 6$  km farther from the COM than is the north pole. (The USGS DEMs assumed a mass-centered reference ellipsoid, and the display of topography relative to this ellipsoid contributed to the notion that the northern hemisphere of Mars represented a depression in the shape of the planet.)

Using the occultation and lander data, we solved for an eighth-degree, and order spherical harmonic model for the shape of Mars (Fig. 1B). The radial accuracy varies between 200 and 1200 m, with an rms error of 500 m with respect to Mars's COM (compared with 1 to 3 km in the USGS DEMs). To remove the rotation-induced oblateness from the global shape, we determined the ellipsoidal heights, that is, the difference between the occultation radii and the best-fit reference ellipsoid (Fig. 1C). There is no elevation difference between the northern and southern hemispheres, although two prominent impact basins, Hellas and Isidis, are evident (Fig. 1C). The ellipsoidal heights are unimodally distributed (Fig. 2A), with excursions resulting from the vast volcano-tectonic

Tharsis rise (which makes up  $\sim 25\%$  of the surface area of Mars) and the 1800-km-diameter Hellas basin. The distribution implies that there is no systematic difference in ellipsoidal heights between the northern and southern hemispheres. However, when the radius of the martian geoid or gravitational equipotential surface (Fig. 1D) is subtracted from the planetary radius, the resulting geopotential topography shows that the northern and southern hemispheres have different elevations (Fig. 1E). The systematic difference of the elevations is evident in the bimodal distribution of topography (Fig. 2B).

Our results indicate that, at the resolution provided by our model, the topography is smooth across the northern and southern hemispheres and across the mapped geologic boundary. Thus, a topographic depression in the northern hemisphere is not a fundamental feature of the shape of Mars, but rather arises when the shape is referenced to the gravity field. The break in topography between the southern and northern hemispheres that arises in the geopotential reference frame does not everywhere correspond to the mapped geologic boundary (Fig. 1A), and it is not as spatially sharp. Instead, it is a gradual change in elevation.

The number and distribution of occultation points near the dichotomy boundary suggested that any sharp elevation changes along the mapped geologic boundary would not necessarily be resolvable from the occultation data set alone. To determine whether the boundary defined by our model is a real feature of Mars, rather than a consequence of undersampling of the boundary, we exam-

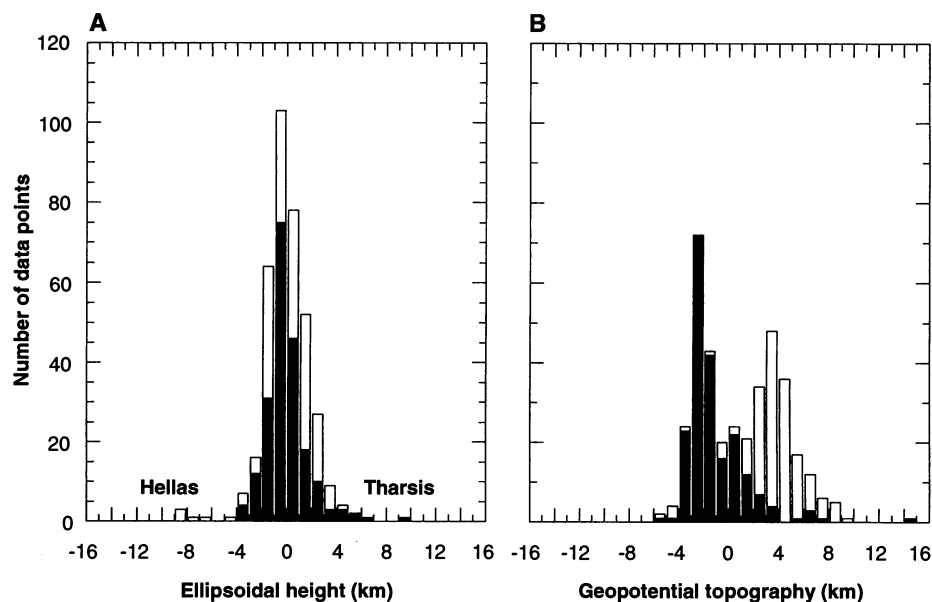


**Fig. 2.** Histograms of ellipsoidal heights (A) and geopotential topography (B) of Mars (solid bars, northern hemisphere; open bars, southern hemisphere). Each column in the histogram is the sum of both hemispheres. Data points are from Viking 1 (93), Viking 2 (47), Mariner 9 (228), and Viking landers (2). The northern hemisphere rms deviations are 2.1 km in (A) and 2.7 km in (B); those for the southern hemisphere are 1.7 km in (A) and 2.4 km in (B). The overall rms deviations are 1.9 km for (A) and 3.5 km for (B).

ined high spatial resolution radar-derived topographic profiles across the geologic boundary. Earth-based radar observations (32–34) provide a direct measure of the distance from Earth to the surface of Mars and, by inference, the radius of Mars. The distance to the point on the surface normal to the incoming wave can be measured to within 10 to 30 km

in longitude and 80 to 120 km in latitude, depending on the distance of Mars from Earth and on transmitter power (34). Because of the limitations in the variation in geometry of the orbit of Mars and its spin axis direction from Earth, radar observations are generally limited to within  $\sim 25^\circ$  of the Mars equator. A typical observation period

produces radar returns from a strip of almost constant latitude (33) with a range precision of better than 100 m (34). Although the radar observations do not provide global coverage, they provide many continuous profiles near the equator and across the geologic boundary.

We examined all radar profiles collected at Mars oppositions during the period 1971–1982 that cross the geologic boundary. Overall, the topography derived from our global occultation model agreed well with the regional radar data sets (Fig. 3A) (35). Only two profiles displayed obvious topographic scarps, and even these features had relatively modest slopes of  $1.2^\circ$  and  $1.7^\circ$  (Fig. 3, B and D). Both scarps were interpreted to have an erosional origin (2). The remaining profiles did not display any sharp change in topography at the geologic boundary (Fig. 3C). Analyses of our topographic model (Fig. 1E) and the radar profiles indicate that the average slope in the north-south direction is  $\sim 0.1^\circ$  between  $15^\circ\text{N}$  and  $15^\circ\text{S}$ . East-west slopes are variable, with an rms magnitude of  $\sim 0.2^\circ$  per  $20^\circ$  of longitude.

A long wavelength, gradual surface slope would be expected to result from the offset of the planet's COM from its center of figure (COF) (Fig. 4). A comparison of the occultation-derived and radar-derived topography as a function of latitude appears to fit such a long wavelength trend, except for deviations caused by major structures such as Tharsis and Hellas (Fig. 4). Thus, our results indicate that the apparent topographic difference between the northern and southern hemispheres reflects the COM-COF offset, and there is no obvious surface depression in the northern hemisphere. However, the distribution of geopotential elevations indicates that the abundant water once present on the martian surface would have flowed from the southern to the northern hemisphere, consistent with the direction implied by massive outflow channels (2).

The distribution of geopotential topography may reflect the variations in the thickness of the crust, because plausible variations in crustal or mantle density cannot explain the observations. The topographic dichotomy is in most places a shallow surface sloping downward to the north rather than a steep decline, even in areas where the planet's geology changes abruptly (2, 4). Small portions of the geologic boundary that display narrow, steeper scarps (18) may define areas of localized erosion that may have occurred as much as an eon after the dichotomy formed (36), and thus they may not be directly relevant to the formation of the boundary. Moreover, the lack of a clearly defined gravity signal associated with the boundary is consistent with the idea that the

**Fig. 3.** (A) Comparison of geopotential elevations from occultation points (▼) and the Viking Lander-1 site (●) with those from Earth-based radar profiles (gray dots) collected during the 1980 and 1982 oppositions. (B through D) Examples of Earth-based radar profiles of geopotential topography that cross the geologic dichotomy boundary in a nearly perpendicular sense. Marked locations of the boundary are taken from the USGS Geologic Map (4). In all profiles, topographic slopes are enhanced by a vertical exaggeration of  $\sim 36:1$ .

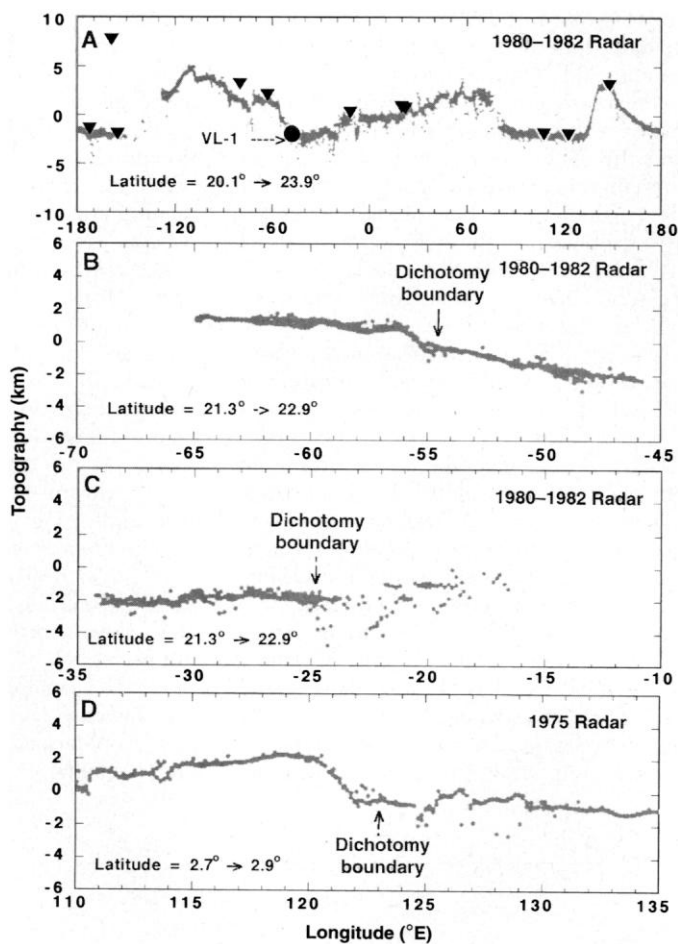
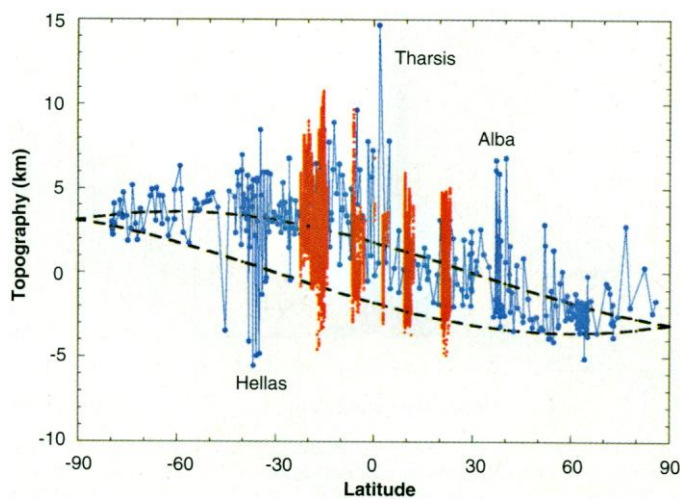


**Fig. 4.** Dynamic range of geopotential topography plotted versus latitude for the occultation data (blue dots) and the Earth-based radar data (red dots). The radar data consist of 45,842 points that represent nearly all observations collected between 1971 and 1982. The radar data appear in bands because measurements are collected along lines of constant latitude. For comparison, the dashed black lines show profiles of the maximum and minimum topography along the longitude lines expected as a result of Mars's COM-COF offset. Note that the occultation and radar topography follow this long wavelength trend.



dichotomy is a consequence of the COM being displaced from the COF, and it does not require a period of global isostatic adjustment during the planet's evolution. (A body with a 700-km-wide, 3-km-high scarp would not have the appearance of a broad, gradual, continuous slope when sampled at the resolution of our model.)

Our assessment of global topography will need to be taken into consideration in future evaluation of models of the origin of northern-southern hemisphere difference on Mars. It is uncertain how the convection models produce a global pattern of long wavelength topography and crustal thickness (37) during contemporaneous accretion and core formation (38). Impact models must be consistent with virtually complete viscous relaxation of impact depressions while maintaining a hemispheric-scale variation in crustal thickness. Plate tectonic models (16), although not inconsistent with the observed range of slopes, must explain relatively complex early plate arrangements in the context of the observed global-scale shape and lack of gravity anomalies associated with the boundary. COM-COF offsets have been observed for the moon and all of the terrestrial planets (39) and have been interpreted (though not uniquely) in terms of global-scale crustal thickness variations. The commonality or diversity in the origin of compositional differentiation at this scale represents one of the outstanding questions in comparative planetology, and analyses of long wavelength topography and gravity can lead to considerable elucidation of this problem.

## REFERENCES AND NOTES

1. T. A. Mutch, R. E. Arvidson, J. W. Head, K. L. Jones, R. S. Saunders, *The Geology of Mars* (Princeton Univ. Press, Princeton, NJ, 1976).
2. M. H. Carr, *The Surface of Mars* (Yale Univ. Press, New Haven, CT, 1981).
3. R. P. Sharp, L. A. Soderblom, B. C. Murray, J. A. Cutts, *J. Geophys. Res.* **76**, 331 (1971); R. P. Sharp, *ibid.* **78**, 4073 (1973).
4. D. H. Scott and K. L. Tanaka, *USGS Map I-1802-A* (1986); R. Greeley and J. E. Guest, *USGS Map I-1802-B* (1987).
5. D. E. Wilhelms and S. W. Squyres, *Nature* **309**, 138 (1984).
6. M. H. Carr, *Icarus* **68**, 187 (1986).
7. S. W. Squyres, *ibid.* **34**, 600 (1978); *J. Geophys. Res.* **84**, 8087 (1979).
8. S. S. C. Wu, R. Jordan, F. J. Schaefer, *NASA Tech. Memo. 88383* (1986), p. 614; S. S. C. Wu, *USGS Map I-2030* (1989); *USGS Map I-2160* (1991).
9. G. F. Davies and R. E. Arvidson, *Icarus* **45**, 339 (1981).
10. R. E. Lingenfelter and G. Schubert, *Moon* **7**, 172 (1973); D. U. Wise, M. P. Golombek, G. E. McGill, *Icarus* **35**, 456 (1979); *J. Geophys. Res.* **84**, 7934 (1979); G. E. McGill and A. M. Dimitriou, *ibid.* **95**, 12595 (1990).
11. G. E. McGill, *J. Geophys. Res.* **94**, 2753 (1989).
12. H. V. Frey and R. A. Schultz, *Geophys. Res. Lett.* **15**, 229 (1988); R. A. Schultz and H. V. Frey, *J. Geophys. Res.* **95**, 14175 (1990).
13. V. R. Baker *et al.*, *Nature* **352**, 589 (1991).
14. W. L. Sjogren, *Science* **203**, 1006 (1979).
15. R. J. Phillips, *EOS Trans. Am. Geophys. Union* **69**, 389 (1988).
16. N. H. Sleep, *J. Geophys. Res.* **99**, 5639 (1994).
17. P. B. Esposito *et al.*, in *Mars*, H. H. Kieffer, B. M. Jakosky, C. W. Snyder, M. S. Matthews, Eds. (Univ. of Arizona Press, Tucson, 1992), pp. 209–248; M. T. Zuber *et al.*, *J. Geophys. Res.* **97**, 7781 (1992).
18. L. A. Soderblom and D. B. Wenner, *Icarus* **34**, 622 (1978); T. J. Parker, R. S. Saunders, D. M. Schneebberger, *ibid.* **82**, 111 (1989).
19. A. J. Kliore, D. L. Cain, G. Fjeldbo, B. L. Seidel, M. J. Sykes, *ibid.* **17**, 484 (1972).
20. A. J. Kliore, F. J. Fjeldbo, B. L. Seidel, M. J. Sykes, P. M. Woiceshyn, *J. Geophys. Res.* **78**, 4331 (1973).
21. E. J. Christensen, *ibid.* **80**, 2909 (1975).
22. G. F. Lindal *et al.*, *ibid.* **84**, 8443 (1979).
23. The principal sources of error in the occultation data include the spacecraft position at the kilometer level (22), the timing of the loss of signal at the 0.1-s level (corresponding to a distance of ~1 km), and the location of the grazing ray at the time of occultation (due to ephemeris errors, geodetic positioning uncertainties, and local topography) (19). Depending on the orbital radius of the spacecraft at the time of occultation, the geometry of the spacecraft and planet, and the topography of the limb, these errors have amounted to several kilometers in planetary radii (19–22).
24. B. G. Bills and A. J. Ferrari, *J. Geophys. Res.* **83**, 3497 (1978).
25. Determination of a planetary radius from occultation data requires precise knowledge of the spacecraft orbit. The uncertainty in the spacecraft orbit is frequently the largest source of error in the calculated radius. The original orbits for the Mariner 9 and Viking occultation measurements had radial accuracies of 1 to 3 km. To improve the estimation of the martian gravity field (28), we recalculated nearly all of the orbits for the Mariner 9 and Viking Orbiters. We used the GEODYN/SOLVE system of orbital analysis programs, which numerically integrate the spacecraft Cartesian state and force model partial derivatives by using a high-order predictor-corrector model. The force modeling includes a spherical harmonic representation of the planet's gravity field, as well as point mass representations for the sun, Earth, and other planets. Solar radiation pressure, atmospheric drag on the spacecraft, tidal parameters, planetary rotation measurement and timing biases, and tracking station coordinates are estimated along with spacecraft orbits. This analysis made use of improved planetary ephemerides (DE234), reference models (J2000), and parameters of the planetary coordinate system. We have improved the radial accuracy of spacecraft orbits with respect to Mars's COM by approximately an order of magnitude, from  $\geq 1$  km to ~100 to 300 m (28).
26. Planetary ephemeris errors resulted in incorrect placement of the planet (by kilometers) at the time of the occultation (circa 1971); although the spacecraft position is with respect to the planet, and to first order the errors cancel, some small fraction of the error remains. Also, knowledge of the rotation of Mars has improved since the 1970s (40), and thus the position of the occultation point can be improved, principally in longitude, to ~500 m.
27. Atmospheric refraction causes the ray path of the radio signal to bend around the planet and change the apparent radius. For Mars, the magnitude of this refraction by the 6-mbar atmosphere is on average slightly less than 0.01°, and it contributes ~150 m of error in the radius of the planet for every 1000 km of spacecraft distance from the occultation point. Because the Mariner 9 and Viking spacecraft altitudes varied from 300 to 30,000 km, atmospheric refraction was a major potential error source. To correct the Viking data, we used refraction angles obtained from the original data (provided by G. Lindal). For the Mariner 9 data, we estimated the atmospheric refraction angle  $\alpha$  from  $\alpha = (8.429 \times 10^{-2})PT^{-3/2}$ , where  $P$  and  $T$  are atmospheric pressure and temperature, respectively. This expression (provided by D. Hinson) assumes a constant atmospheric temperature and is estimated to be valid to ~10% for small refraction angles. The largest refraction corrections occurred at high latitudes, where the spacecraft were typically more distant from Mars. Refraction corrections to the radius were typically on the order of 1 to 2 km, but the largest was 12 km. The single largest source of error is the orbit at ~400 m; the next largest is atmospheric refraction at ~300 m, followed by occultation timing and planetary ephemeris errors. The total root sum square error of a typical occultation is estimated to be a little over 500 m. The error model for the atmospheric refraction was ~10% of the total correction.
28. D. E. Smith *et al.*, *J. Geophys. Res.* **98**, 20871 (1993).
29. J. Lorell *et al.*, *Icarus* **18**, 304 (1973).
30. The Viking landers contained atmospheric pressure sensors that have also been used to calculate relative surface elevation. These sensors measured pressure directly, so the Viking sites have the best-determined relative elevations on Mars. However, these measurements were not included in the USGS DEM. A comparison of the relative heights of these sites shows them to disagree with the lander site elevations in the DEM by ~2 km and to be in the incorrect relative direction with respect to each other (41). In our geopotential topography model, the relative elevations of the sites agree with relative heights derived from the lander pressure data to within 49 m, and they are in the correct direction with respect to each other.
31. Our best-fit ellipsoid is triaxial with semimajor axis  $A = 3399.472$  km, intermediate semimajor axis  $B = 3394.329$  km, and semiminor axis  $C = 3376.502$  km, with an inverse flattening ( $1/f$ ) of 166.53. The offset of the COF from the COM is  $x = -130$  m,  $y = -1780$  m, and  $z = -3081$  m. The  $A$  axis of our ellipsoid is 4.9 km greater than that of the USGS DEM, and the  $B$  and  $C$  axes are greater by 1.0 km and 200 m, respectively.
32. G. S. Downs, R. M. Goldstein, R. R. Green, G. A. Morris, P. E. Reichley, *Icarus* **18**, 8 (1973); G. S. Downs, P. E. Reichley, R. R. Green, *ibid.* **26**, 273 (1975).
33. L. E. Roth, G. S. Downs, R. S. Saunders, G. Schubert, *ibid.* **42**, 287 (1980).
34. G. S. Downs, P. J. Mougins-Mark, S. H. Zisk, T. W. Thompson, *J. Geophys. Res.* **87**, 9747 (1982).
35. The primary source of error for the radar data is the planetary ephemeris (42); this error, combined with a lesser error induced by solar plasma effects, indicates a vertical accuracy of ~300 m for these measurements, which is comparable to that of the occultation data. However, the radar measurement is an average for an area of several square kilometers, whereas the occultation measurement is a point location. Thus, a systematic difference between the radii derived from the two data sets might be expected. In a comparison of the topography derived from the radar data with that derived from the occultation data, a systematic difference in radius was detected, with a mean of  $730 \pm 173$  m; the radar-derived radii were smaller than the occultation radii. The sign of this difference is consistent with the radar data, providing a measure of the planetary radius to the floors of valleys, and with the occultation data, providing a measure of the planetary radius to the higher topographic locations, such as mountains.
36. G. E. McGill and S. W. Squyres, *Icarus* **93**, 386 (1991).
37. M. T. Zuber, D. E. Smith, G. A. Neumann, in preparation.
38. C.-Y. Shih *et al.*, *Geochim. Cosmochim. Acta* **46**, 2323 (1982); G. Schubert, S. C. Solomon, D. L. Turcotte, M. J. Drake, N. H. Sleep, in *Mars*, H. H. Kieffer, B. M. Jakosky, C. W. Snyder, M. S. Matthews, Eds. (Univ. of Arizona Press, Tucson, 1992), pp. 147–183.
39. G. Balmino, K. Lambeck, W. M. Kaula, *J. Geophys. Res.* **78**, 478 (1973); D. L. Bindshadler, G. Schubert, P. G. Ford, *Icarus* **111**, 417 (1994); M. T. Zuber, D. E. Smith, F. G. Lemoine, G. A. Neumann, *Science* **266**, 1839 (1994); J. D. Anderson, R. F. Jurgens, E. L. Lau, M. A. Slade, G. Schubert, in preparation.
40. A. P. Mayo *et al.*, *J. Geophys. Res.* **82**, 4297 (1977); W. H. J. Michael, *Moon Planets* **20**, 149 (1979); N. Borderies, G. Balmino, L. Castel, B. Moynot, *ibid.* **22**, 191 (1980); G. Balmino, B. Moynot, N. Vales, *J. Geophys. Res.* **87**, 9735 (1982).
41. H. H. Kieffer, B. M. Jakosky, C. W. Snyder, in *Mars*, H. H. Kieffer, B. M. Jakosky, C. W. Snyder, M. S. Matthews, Eds. (Univ. of Arizona Press, Tucson, 1992), pp. 1–33.
42. E. M. J. Standish, "The JPL Planetary and Lunar

Ephemerides, DE234/LE234" (Jet Propulsion Laboratory Interoffice Memorandum 314.6-1348, 1991). We thank S. Asmar and M. Connolly for "rediscovering" the Viking occultation data in an unmarked file cabinet at the Jet Propulsion Laboratory, G. Lindal for providing the refraction angles used to correct the Viking data, D. Hinson for helpful discussions regarding atmospheric corrections to the occultation data, D. Rowlands for software support in the processing of occultations, S. Fricke for orbital computations, J. Finnochiario for assistance with atmospheric refraction corrections, R. Jurgens and M. Slade for radar

data, F. Lemoine for assembling geoid values used to determine geopotential topography, G. Neumann for assistance with Fig. 1, S. Solomon for discussions about interpretation of the results, and N. Sleep and an anonymous referee for helpful reviews. The Mariner 9 data (A. Kliore, principal investigator) were obtained from the National Space Science Data Center at the Goddard Space Flight Center. Supported by the NASA Planetary Geology and Geophysics Program and the NASA Mars Global Surveyor Project.

25 September 1995; accepted 4 December 1995

## Permian Vessel Elements

Hongqi Li, Edith L. Taylor,\* Thomas N. Taylor

Anatomically preserved stems from the Late Permian (250 to 270 million years ago) of China have been discovered that contain vessels. The stems possess several features commonly found in vines, including tendril-like appendages, and are associated with large leaves assignable to the Gigantopteridales, an enigmatic group of Permian plants. The individual vessel elements contain foraminate perforation plates in their end walls and are anatomically similar to the conducting elements of modern gnetophytes and of some extant flowering plants.

Tracheids and vessels are the two principal types of water-conducting cells in vascular plants. Tracheids are generally elongate cells with imperforate end walls, whereas vessels consist of a series of individual members joined by perforate end walls. As water moves through a vertical series of tracheids, it must move through primary wall material at the end of each cell. Because of their perforated end walls, however, vessels allow barrier-free water movement and thus result in a considerably more efficient water conduction system. Although vessels have been reported in a few vascular cryptogams (1), for the most part they are characteristic of angiosperms. Vessels have been documented in fossil angiosperms as early as the Lower Cretaceous (Albian) (2) but had not been found in other groups of fossil plants. Here we describe vessel-bearing plants from the Upper Permian of western Guizhou Province, China. They are preserved as calcium carbonate permineralizations and were studied by means of cellulose acetate peels for light microscopy or as fractured stem sections for scanning electron microscopy.

The stems are slender, typically less than 1 cm in diameter, and are characterized by elongate tendril-like appendages extending from the epidermis. Surrounding the central pith are five to nine fan-shaped, mesarch, primary xylem segments, each bordered by a zone of secondary xy-

lem to the outside (Fig. 1). Protoxylem tracheids possess annular to helical secondary wall thickenings, whereas the metaxylem elements range from reticulate-scalariform pitting to circular bordered pits. Secondary xylem elements consist of a small number of vessels on the inside of the stem and several rows of tracheids toward the periphery. Extending through the secondary xylem are vascular rays that are 1 to 2 cells wide and up to 60 cells high.

Within the secondary xylem, tracheids are triangular-rectangular in cross section and from 50 to 90  $\mu\text{m}$  in diameter; side walls possess circular bordered pits, each approximately 9  $\mu\text{m}$  in diameter. Vessels vary from 150 to 300  $\mu\text{m}$  in diameter; a



Fig. 2. Transverse section showing two vessel elements with perforation plate (arrow) between them. Width of photograph, 66 mm.

few near the stem center are nearly 500  $\mu\text{m}$  in diameter (Fig. 2). Vessel elements are 5 to 7 mm long, with end walls that are generally oblique (Fig. 3). A few are shorter and possess end walls that are nearly perpendicular. Each end wall consists of a multiperforate perforation plate with approximately 14 rows of circular perforations (Fig. 4), each approximately 14 to 16  $\mu\text{m}$  in diameter. Perforations near the margin of the perforation plate are slightly smaller, and typically the primary cell wall material is incompletely dissolved within the perforation (Fig. 5). The side walls of these Permian vessels exhibit multiple rows of circular-to-oval bordered pits, and these are generally less than 10  $\mu\text{m}$  in diameter.

In the same blocks as the permineralized stems are numerous leaves assignable to *Gigantopteris* and *Gigantonoclea*, two leaf morphotypes included in the Gigantopteridales (3). Although the gigantop-



Fig. 1. Transverse section of a wedge of secondary xylem showing tracheids and large vessels. Width of photograph, 70 mm.



Fig. 3. Longitudinal section of vessel showing oblique end wall (arrow). Width of photograph, 66 mm.

H. Li, Department of Plant Biology, Ohio State University, Columbus, OH 43210, USA.

E. L. Taylor and T. N. Taylor, Department of Botany and Museum of Natural History, University of Kansas, Lawrence, KS 66045-2106, USA.

\*To whom correspondence should be addressed.